J/M PAPERS

Mesoscopic models for electrohydrodynamic interactions of polyelectrolytes

Dmitry I. Kopelevich[1],†, **Shujun He**[1], **Ryan J. Montes**[1] **and Jason E. Butler**[1]

[1]Department of Chemical Engineering, University of Florida, Gainesville, FL 32611-6005, USA

Two mean-field models for polyelectrolytes in simultaneous electric field and pressure-driven flow field were developed and compared. The models predict migration perpendicular to the anti-parallel or parallel fields, where the migration is caused by electrohydrodynamic interactions calculated using either a short- or long-range approximation. Inputs for the mean-field models were determined from Brownian dynamics simulations in a simple shear flow. Both models qualitatively reproduce experimental observations of DNA focusing as reported in previous publications. Specifically, it is observed that combination of the shear and electric fields leads to polyelectrolyte motion in the direction transverse to the flow and electric field direction, which in turn leads to concentration of the polyelectrolyte in the centre of a microfluidic channel. Furthermore, both models predict that there is an optimal strength of electric field that leads to the narrowest distribution profile of the polyelectrolyte in the centre of the channel. The analysis suggests that this is due to dispersion induced by the electrohydrodynamic interactions. However, quantitative disagreement between the model predictions and the experimental data indicates that further progress in the model development is needed.

Key words: microfluidics, polymers

1. Introduction

Parallel application of a pressure-driven flow and electric field can drive a net migration of long DNA strands to the walls of a capillary, and reversing the relative directions of the flow and electric field causes the DNA strands to migrate towards the centre of the capillary (Zheng & Yeung 2002, 2003; Arca, Butler & Ladd 2015). This transverse migration has been used to trap and concentrate DNA within a microfluidic chip of simple design, and evidence suggests that the process can separate DNA from other macromolecules and particulates (Arca, Ladd & Butler 2016; Montes, Butler & Ladd 2019*a*; Valley *et al.* 2020).

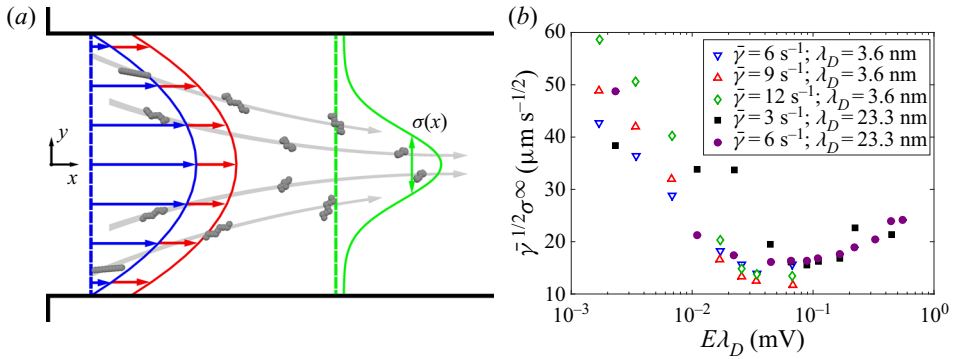† Email address for correspondence: dkopelevich@che.ufl.edu

Figure 1. (*a*) Applying an electric field $\boldsymbol{E}$ anti-parallel to a pressure-driven flow (blue) causes an initially uniform distribution of DNA, which is negatively charged, to lead the flow (red) and migrate towards the centre of the channel (grey field). The width of the concentration profile (green) is characterized by the standard deviation $\sigma(x)$ corresponding to the concentration profile $C(y|x)$ at position x. (*b*) Dependence of widths $\sigma^\infty = \sigma(x \to \infty)$ of the developed concentration profiles of DNA molecules in a microfluidic channel on the electric field E obtained in the experiments of Arca *et al.* (2015) for several mean shear rates $\bar{\gamma}$ and Debye lengths λ_D. The normalization for the axes was chosen to collapse the data onto a single curve.

The transverse migration of DNA strands has been attributed to intramolecular velocity disturbances caused by the electric field acting on the charged backbone of the polyelectrolyte and its surrounding counterion cloud (Butler *et al.* 2007; Usta, Butler & Ladd 2007; Kekre, Butler & Ladd 2010*b*; Pandey & Underhill 2015; Ladd 2018). These electrohydrodynamic interactions are commonly ignored when calculating the electrophoretic motion of DNA and other polyelectrolytes. However, these interactions can alter the motion if the electric double layer is large in comparison with the backbone cross-section and the DNA molecule is distorted from its equilibrium (roughly spherical) configuration. In the case of migration during a pressure-driven flow, hydrodynamic forces stretch the DNA molecule within the extensional quadrants of the local shear flow. Then, the electric field and resulting electrohydrodynamic interactions induce additional components of motion, including one transverse to the flow and field direction. When a flexible polyelectrolyte leads a pressure-driven flow upon application of an axial electric field, the transverse motion is towards the centre of the channel, as illustrated in figure 1(*a*); upon reversing the electric field direction, the same polyelectrolyte will lag the flow and move towards the bounding walls.

Two different approximations for electrohydrodynamic interactions have been employed to calculate the centre-of-mass distribution of bead–spring models of polyelectrolytes. The long-range model (Butler *et al.* 2007; Kekre *et al.* 2010*b*) treats each bead as a uniformly distributed collection of point charges, where each point charge is surrounded by counterions. The velocity disturbances caused by the electric field acting on the point charges and counterions within each bead are calculated using the algebraically decaying terms in the Green's function, while ignoring the exponentially decaying terms (Allison & Stigter 2000; Long & Ajdari 2001). The net velocity disturbance from each bead is summed pairwise over all other beads of the polymer, but velocity disturbances within the beads are ignored.

The other model assumes that the electrohydrodynamic interactions are localized to individual Kuhn steps (Liao *et al.* 2010; Pandey & Underhill 2015; Ladd 2018). This short-range approximation uses the electrophoretic mobility of rigid rods (Chen & Koch 1996) to represent the motion of each Kuhn step. Rigid rods can move perpendicular to the electric field if the Debye length is sufficiently large and the rods are aligned at an

angle with respect to the electric field. The mobility tensor relating the electric field to the motion of each bead of the polymer is obtained by averaging over the mobilities of the rods composing it. Like the long-range model, transverse motions to the flow and field are predicted only if the polyelectrolyte is distorted from its equilibrium configuration and if the electric double layer is sufficiently large with respect to the polymer backbone size.

The proposed mechanism of electrohydrodynamic migration has been validated, at least qualitatively, against experimental observations of DNA migration. For example, experiments (Arca *et al.* 2015; Montes, Ladd & Butler 2019*b*) demonstrated that migration can be eliminated by increasing the buffer salt concentration, which reduces the double-layer thickness and screens the electrohydrodynamic interactions. Some alternative mechanisms were also investigated by Montes *et al.* (2019*b*) and were found to be inadequate to explain the observed migration. Additionally, experiments with anti-parallel fields (Arca *et al.* 2015) indicate that DNA initially focuses more strongly in the centre of the channel with increasing electric field, but focusing diminishes once a critical electric field is surpassed (see figure 1*b*). Brownian dynamics simulations using the long-range approximation predicted this increase and subsequent decline of concentration upon increasing the electric field (Kekre *et al.* 2010*b*). Simulations using the short-range approximation (Pandey & Underhill 2015) also predict an increase in concentration for weak fields, and more recent analysis (Setaro & Underhill 2019) also suggests that the concentration declines as the electric field increases beyond a critical value.

Quantitative differences between the models and the experimental results are evident from previous studies (Kekre *et al.* 2010*b*; Pandey & Underhill 2015; Ladd 2018), but assessing the relative merits of the short- and long-range approximations is difficult due to the different parameters used. Here we report a mean-field model for a polyelectrolyte in a pressure-driven flow and an electric field which causes the polyelectrolyte to lead the flow, and hence migrate towards the centre of the channel. The model is a convection–diffusion equation with diffusion tensor and convective velocities obtained from Brownian dynamics simulations in a simple shear flow, and the mean-field model is also validated using Brownian dynamics simulations in parabolic flows. Mean-field models with the short-range and long-range approximations of the electrohydrodynamic interactions were considered.

Comparing the results with the experiments of Arca *et al.* (2015) provides a number of conclusions regarding the models. Among them, predicting the observed migration requires setting the Debye length to a value much larger than in the experiments for the long-range model, as previously determined (Ladd 2018). The short-range model predicts significant migration even when the Debye length is comparable to that in the experiments, but the electric field at which focusing diminishes is much larger than measured in experiments. Also, analysis demonstrates that dispersion caused by the coupling of fluctuations of the polymer configuration and electric field causes the maximum in the extent of migration. Furthermore, the experimentally observed scaling of the width σ^∞ of the developed concentration profile with the mean shear rate $\bar{\gamma}$ ($\sigma^\infty \propto \bar{\gamma}^{-1/2}$; see figure 1*b*) is explained. These results and conclusions are discussed in §§ 3–5, following presentation of the relevant theoretical background and numerical methods in § 2.

2. Theoretical background and model development

2.1. *Model*

We consider a DNA molecule in an ambient flow field $\boldsymbol{u}^\infty(\boldsymbol{r})$ and a uniform electric field $\boldsymbol{E}$. The molecule is modelled as a chain of N beads with coordinates $\boldsymbol{r}_1, \boldsymbol{r}_2, \ldots, \boldsymbol{r}_N$ connected by $N-1$ springs. The dynamics of the DNA beads is described by the Langevin

equation:

$$\frac{\mathrm{d}\boldsymbol{r}_i}{\mathrm{d}t} = \boldsymbol{u}^\infty(\boldsymbol{r}_i) + \sum_{j=1}^{N} \boldsymbol{\mu}_{ij}^H \cdot (\boldsymbol{F}_j^C + \boldsymbol{F}_j^B) + \mu_0^E \boldsymbol{E} + \boldsymbol{v}_i^E. \tag{2.1}$$

Here, $\boldsymbol{F}_i^C$ and $\boldsymbol{F}_i^B$ are the conservative and Brownian forces acting on bead i, $\boldsymbol{\mu}_{ij}^H$ is the mobility tensor which includes hydrodynamic interactions, μ_0^E is the electrophoretic mobility in the absence of shear and $\boldsymbol{v}_i^E$ is the velocity disturbance due to electrohydrodynamic interactions.

The conservative force includes the spring force $\boldsymbol{F}_i^S$, the bead–bead repulsion force $\boldsymbol{F}_i^R$ and the bead–wall repulsion force $\boldsymbol{F}_i^W$:

$$\boldsymbol{F}_i^C = \boldsymbol{F}_i^S + \boldsymbol{F}_i^R + \boldsymbol{F}_i^W. \tag{2.2}$$

The springs connecting the beads represent freely jointed chains of N_K Kuhn steps of length l_K, with the tension approximated by the finitely extensible nonlinear elastic (FENE) force (Warner 1972):

$$\boldsymbol{F}_i^S = -\sum_j \frac{\kappa \boldsymbol{r}_{ij}}{1 - (r_{ij}/r_0)^2}. \tag{2.3}$$

Here, the summation is performed over beads $j = i \pm 1$ connected to bead i, $\boldsymbol{r}_{ij} = \boldsymbol{r}_i - \boldsymbol{r}_j$ is the vector connecting beads j and i, r_{ij} is the magnitude of $\boldsymbol{r}_{ij}$, $\kappa = 3k_B T/l_K r_0$ is the spring constant, k_B is the Boltzmann constant, T is the temperature and $r_0 = N_K l_K$ is the maximum spring extension.

Excluded volume between beads is enforced using a repulsive force with potential (Kekre, Butler & Ladd 2010a)

$$\Phi^R(r_{ij}) = A \exp(-\beta r_{ij}^2), \tag{2.4}$$

where parameters A and β specify the force magnitude and range. Simulations of polymers in pressure-driven flows also include a repulsive force to prevent polymer beads from passing through the channel walls. The potential energy of interaction between each bead i and the bounding walls is

$$\Phi^W(d_{ij}) = 2A \exp(-\beta(d_{ij} - a)^2), \tag{2.5}$$

where a is the bead radius and d_{ij} is the distance between the bead centre and wall j.

Brownian forces acting on the polymer beads satisfy the fluctuation–dissipation theorem:

$$\left.\begin{array}{l} \langle \boldsymbol{F}^B(t) \rangle = 0, \\ \langle \boldsymbol{F}^B(t) \boldsymbol{F}^B(t+\tau) \rangle = 2k_B T (\boldsymbol{\mu}^H)^{-1} \delta(\tau), \end{array}\right\} \tag{2.6}$$

where $\boldsymbol{F}^B = (\boldsymbol{F}_1^B, \boldsymbol{F}_2^B, \ldots, \boldsymbol{F}_N^B)$ is the $3N$-dimensional vector containing Brownian forces acting on all of the beads, $\boldsymbol{\mu}^H$ is the $3N \times 3N$ grand mobility tensor and δ is the Dirac delta function.

The Rotne–Prager tensor is used to describe the hydrodynamic interactions between individual beads (Rotne & Prager 1969):

$$\boldsymbol{\mu}_{ij}^{H}(\boldsymbol{r}_{ij}) = \frac{1}{\zeta} \begin{cases} \boldsymbol{I}, & i = j, \\ C_1(r_{ij})\boldsymbol{I} + C_2(r_{ij})\hat{\boldsymbol{r}}_{ij}\hat{\boldsymbol{r}}_{ij}, & i \neq j, \end{cases} \tag{2.7}$$

where $\zeta = 6\pi\eta a$ is the drag coefficient, η is the fluid viscosity, $\hat{\boldsymbol{r}}_{ij} = \boldsymbol{r}_{ij}/r_{ij}$ is the unit vector pointing from bead j to bead i and

$$C_1(r_{ij}) = \begin{cases} \dfrac{3a}{4r_{ij}} + \dfrac{a^3}{2r_{ij}^3}, & r_{ij} \geq 2a, \\ 1 - \dfrac{9r_{ij}}{32a}, & r_{ij} < 2a, \end{cases} \qquad C_2(r_{ij}) = \begin{cases} \dfrac{3a}{4r_{ij}} - \dfrac{3a^3}{2r_{ij}^3}, & r_{ij} \geq 2a, \\ \dfrac{3r_{ij}}{32a}, & r_{ij} < 2a. \end{cases} \tag{2.8a,b}$$

Hydrodynamic interactions between beads and walls were neglected. Kekre *et al.* (2010*b*) demonstrated that these interactions have a negligible effect on the developed concentration profile for the case studied here, where the channel dimension is much larger than the polyelectrolyte and the polyelectrolyte migrates towards the centre of the channel.

2.2. *Models of electrohydrodynamic interaction*

Two alternative approaches to modelling electrohydrodynamic interactions ($\boldsymbol{v}_i^E$) were investigated. The long-range model (Butler *et al.* 2007; Kekre *et al.* 2010*b*) assumes that each bead of the polymer model represents a blob of uniformly distributed charges and utilizes the Green's function for the velocity field caused by an electric field acting on a point charge and its surrounding counterion cloud (Allison & Stigter 2000; Long & Ajdari 2001). The short-range model (Liao *et al.* 2010; Pandey & Underhill 2015; Ladd 2018) approximates electrohydrodynamic mobilities of each polymer bead by averaging the mobilities of Kuhn steps comprising the bead. The motion due to the electric field of each Kuhn step is approximated as that of a charged rigid rod (Chen & Koch 1996) and electrohydrodynamic interactions between the Kuhn steps are neglected.

As shown in appendix A, the velocity $\boldsymbol{v}_i^E$ of each bead i can be written as

$$\boldsymbol{v}_i^E = \mathcal{E}_m \sum_{j \neq i} \hat{\mu}_{m,ij}^E(r_{ij})\boldsymbol{A}(\hat{\boldsymbol{r}}_{ij}) \cdot \hat{\boldsymbol{E}}, \tag{2.9}$$

where the subscript m indicates the model ($m = L$ for long-range model and $m = S$ for short-range model) and $\hat{\boldsymbol{E}} = \boldsymbol{E}/E$ is the unit vector parallel to the electric field. The parameter $\mathcal{E}_m$ characterizes the strength of the electrohydrodynamic interactions, while $\hat{\mu}_{m,ij}^E(r)$ describes the dependence of the electrohydrodynamic interactions between beads i and j on the distance r between them. The tensor

$$\boldsymbol{A}(\hat{\boldsymbol{r}}_{ij}) = 3\hat{\boldsymbol{r}}_{ij}\hat{\boldsymbol{r}}_{ij} - \boldsymbol{I} \tag{2.10}$$

is zero on average when the distribution of beads is isotropic, i.e. $\langle\hat{\boldsymbol{r}}_{ij}\hat{\boldsymbol{r}}_{ij}\rangle = \boldsymbol{I}/3$. This condition is met in the absence of shear, and on average the electrohydrodynamic interactions between different beads cancel out. Consequently no net migration occurs perpendicular to the electric field in this case, as expected.

For the long-range model, the summation in (2.9) is performed over all $j \neq i$, and the model-dependent parameters in the equations are given by

$$\hat{\mu}_{L,ij}^{E}(r) = \begin{cases} r^{-3}, & r \geq 2a, \\ 0, & r < 2a \end{cases} \tag{2.11}$$

and

$$\mathcal{E}_L = \frac{3a\lambda_D^2 QE}{2\zeta}. \tag{2.12}$$

Here, Q is the charge of a bead and λ_D is the Debye length. For the short-range model, the summation on the right-hand side of (2.9) is performed only over beads $j = i \pm 1$ connected to bead i. The parameters in this case are given by

$$\hat{\mu}_{S,i,i\pm1}^{E}(r) = \frac{2}{N_s(i)} \frac{(r/r_0)^2}{3 - (r/r_0)^2}, \tag{2.13a}$$

where

$$N_s(i) = \begin{cases} 1, & i = 1 \text{ or } i = N, \\ 2, & \text{otherwise}, \end{cases} \tag{2.13b}$$

and

$$\mathcal{E}_S = \frac{1 - \alpha_\mu}{1 + 2\alpha_\mu} \mu_0^E E. \tag{2.14}$$

Here, $N_s(i)$ is the number of springs connected to the ith bead and $\alpha_\mu = \mu_\perp^{E,rod}/\mu_\parallel^{E,rod}$ is the ratio of the Kuhn step (rod) mobility in the directions perpendicular and parallel to the rod axis. The value of α_μ varies between 1/2 and 1, depending on the Debye length λ_D. According to the slender-body model for a cylinder (Chen & Koch 1996), $\alpha_\mu \approx 1/2$ for the range of λ_D considered in the experiment of Arca *et al.* (2015) ($d < \lambda_D < l_K$, where d is the diameter of the rod). For a thin double layer ($\lambda_D \ll d$), the model for an infinitely long cylinder (Ohshima 1996) yields $\alpha_\mu \approx 1$ and $\mathcal{E}_S = 0$. No net migration occurs perpendicular to the electric field in this limit.

2.3. *Model parameters*

Here, λ-DNA molecules are modelled by a chain consisting of 20 beads to facilitate comparison with experiments. Each subchain connecting neighbouring beads corresponds to $N_K = 10$ Kuhn steps of length $l_K = 106$ nm each. The corresponding bead charge obtained from the Manning condensation model (Manning 1969) is $Q = 1493.6e$. Throughout this work, parameter values are normalized using the characteristic length $b = \sqrt{k_B T/\kappa} = l_K \sqrt{N_K/3} = 193.5$ nm, characteristic time $t_c = \zeta/\kappa = 0.0122$ s, characteristic energy $k_B T$ and elementary charge e. With this choice of characteristic values, the dimensionless values of the spring constant κ and the drag coefficient ζ both equal one. Dimensionless values of other model parameters that are kept constant throughout this work are summarized in table 1. These values match those used by Kekre *et al.* (2010a,b), with the exception of the electrophoretic mobility μ_0^E. The value of $\mu_0^E = 120.7$ measured in experiments (Montes 2018) for a buffer with an estimated Debye length $\lambda_D = 0.03$ was used (see § S1 of the supplementary material available at https://doi.org/10.1017/jfm.2021.11).

Additional parameters that characterize the strength of the electrohydrodynamic interactions, such as the Debye length λ_D for the long-range model and the ratio α_μ for the

Parameter	Value
Number of beads	$N = 20$
Hydrodynamic radius of a bead	$a = 0.36$
Maximum extension of the FENE spring	$r_0 = 5.0$
Magnitude of excluded volume interactions (2.4), (2.5)	$A = 2.7$
Parameter of excluded volume potential (2.4), (2.5)	$\beta = 1.8$
Electrophoretic mobility of DNA	$\mu_0^E = 120.7$
Bead charge	$Q = 1493.6$

Table 1. Dimensionless values of the parameters of the λ-DNA model that are kept constant throughout this work.

short-range model, are absorbed into the parameters $\mathcal{E}_L$ and $\mathcal{E}_S$, respectively. These latter parameters are varied systematically in the computations.

It should be noted that the parameters $\mathcal{E}_L$ and $\mathcal{E}_S$ corresponding to the same electric field strength E differ by three orders of magnitude for typical experimental conditions, $\alpha_\mu \approx 1/2$, $\lambda_D = O(10^{-2})$. For these conditions, (2.12) and (2.14) yield

$$\frac{\mathcal{E}_L}{\mathcal{E}_S} \approx \frac{6a\lambda_D^2 Q}{\mu_0^E} = O(10^{-3}). \tag{2.15}$$

2.4. *Brownian dynamics simulations*

Simulations of the Langevin equation (2.1) were performed using the Brownian dynamics method (Ermak & McCammon 1978). Three different flow fields $\boldsymbol{u}^\infty(\boldsymbol{r})$ were investigated, namely pressure-driven flows in two different geometries and a simple shear flow. In all simulations, the flow and electric field were directed along the x axis, which causes the polyelectrolyte to lead the flow since $\mu_0^E > 0$. As a result, transverse migration occurs from regions of high flow rate to regions of low flow rate.

Initial configurations of the bead positions were sampled from simulations in the absence of a flow and electric field, where these equilibrium simulations were long compared to the correlation time of 42 for the end-to-end vector (see § S2 of the supplementary material). Time steps between 10^{-4} and 10^{-3} were used, depending on the shear rate and the strength of the electric field, with stronger rates and fields requiring smaller time steps. The step-size selection was validated by confirming that the structural and transport properties of polymers were consistent with those obtained with simulations using smaller step sizes.

The considered pressure-driven flows were flows between parallel plates separated by a distance H (referred to as the two-dimensional or 2-D flow) and through a channel of cross-section $H \times H$ (referred to as the three-dimensional or 3-D flow). The dimension of $H = 413$ was chosen to match the experiments of Arca *et al.* (2015), and the flow is characterized by the mean shear rate $\bar{\gamma} = 2v_0/H$, where v_0 is the centreline flow velocity. For flows through a square cross-section, $\boldsymbol{u}^\infty(\boldsymbol{r})$ was determined numerically using a finite-difference solution of the Stokes equation for a unidirectional flow and $\boldsymbol{u}^\infty(\boldsymbol{r}_i)$ for each bead was obtained by the bilinear interpolation of the numerically obtained velocity values stored on a square grid.

For each set of conditions (flow and electric fields, geometry), a total of 10^4 bead–spring chains were initially distributed at the entry ($x = 0$) and simulated for a channel length

sufficient to attain a fully developed concentration profile. Concentration profiles $C(\boldsymbol{\rho}|x)$ at various positions x along the channel were computed ($\boldsymbol{\rho}$ represents the transversal coordinates of the polymer centre of mass, $\boldsymbol{\rho} = y$ for 2-D flows and $\boldsymbol{\rho} = (y, z)$ for 3-D flows). The width of the concentration profile in the 2-D channel is characterized by the standard deviation $\sigma(x)$ corresponding to the concentration profile $C(y|x)$ at position x. To obtain the width of the concentration profile in the 3-D channel, the concentration $C(y, z|x)$ was first averaged in the depth (z direction) to obtain a 2-D profile $C_{av}(y|x)$. This was followed by computing the standard deviation $\sigma(x)$ of $C_{av}(y|x)$. This approach was chosen over a more straightforward calculation of the standard deviation of the 3-D concentration profile $C(y, z|x)$ to mimic experimental measurements of Arca *et al.* (2015).

For simple shear flow, at least 2000 trajectories were simulated for each set of parameter values (shear rate and electric field). Each trajectory was simulated for a duration of 5000, but only data for times greater that 500 were used in the analysis. The mean polymer velocity V_c was obtained by fitting the ensemble average of the polymer displacement from its initial equilibrated position to a straight line, $\langle R_c(t)\rangle = V_c t$. The diffusion tensor was obtained from deviations $\boldsymbol{\xi}_c(t) \equiv R_c(t) - V_c t$ of individual trajectories from the mean trajectory by fitting each of the components of the mean-squared displacement tensor $\langle \boldsymbol{\xi}_c(t)\boldsymbol{\xi}_c(t)\rangle$ to a straight line. Both $\langle R_c(t)\rangle$ and $\langle \boldsymbol{\xi}_c(t)\boldsymbol{\xi}_c(t)\rangle$ increase linearly in time (see § S3.1 of the supplementary material), and consequently the motion of the polymer centre of mass can be modelled by a Langevin equation, as described next.

2.5. *Mean-field model*

Results from Brownian dynamics simulations of polyelectrolytes in simple shear flows were used to develop a mean-field model for the polymer distribution in more complex geometries. The model assumes that motion of the polymer centre of mass R_c can be described by the following Langevin equation:

$$\dot{R}_c(t) = \boldsymbol{u}^\infty(R_c) + \mu_0^E E + V_c + \boldsymbol{\Gamma}_c(t), \tag{2.16}$$

where V_c is the mean contribution of the electrohydrodynamic interactions to the velocity of the centre of mass and $\boldsymbol{\Gamma}_c$ is the effective random force acting on the centre of mass. Here $\boldsymbol{\Gamma}_c$ contains contributions from the Brownian force and the fluctuating component of the electrohydrodynamic interactions caused by fluctuations of the polymer configuration. The random force $\boldsymbol{\Gamma}_c$ has a zero mean and covariance

$$\langle \boldsymbol{\Gamma}_c(t)\boldsymbol{\Gamma}_c(t+\tau)\rangle = 2\boldsymbol{D}\delta(\tau), \tag{2.17}$$

where $\boldsymbol{D}$ is the effective diffusion tensor.

Therefore, the polymer concentration $C(r)$ is expected to obey a convection–diffusion equation with position-dependent drift velocity and diffusivity:

$$\frac{\partial C}{\partial t} = \nabla \cdot [\boldsymbol{D}\nabla - (\boldsymbol{u}^\infty + \mu_0^E E + V_c)]C. \tag{2.18}$$

In a simple shear flow, statistics of the polymer configuration are independent of the polymer position and, hence, V_c and $\boldsymbol{D}$ are constant. In a more complex flow geometry, V_c and $\boldsymbol{D}$ are position-dependent, with their value determined by the local shear $\gamma(r)$. The model (2.18) is valid if the memory effects can be neglected, i.e. the polymer instantly acquires its diffusivity and velocity corresponding to the local environment. This assumption holds since the response time of the polymer to changes in the environment is much smaller than the time it takes the polymer to move from one streamline to another.

This is verified by the Brownian dynamics simulations discussed in § 3 and the time-scale analysis presented in § S4.3.1 of the supplementary material.

The mean-field model is applied to pressure-driven unidirectional flows in the same 2-D and 3-D geometries as those considered in the Brownian dynamics simulations. In these systems, the local shear rate $\gamma(\mathbf{r})$ depends only on the transverse coordinates $\boldsymbol{\rho}$ and is independent of the position x along the channel length. Hence, the local drift velocity and diffusivity are also independent of x. Moreover, transport in the x direction is dominated by the convective and electrophoretic velocities and the diffusivity in the x direction can be neglected (see § S4.3.2 of the supplementary material). Assuming furthermore that the system is at steady state, (2.18) can be approximated as

$$(u_x^\infty(\boldsymbol{\rho}) + \mu_0^E E + V_{c,x}(\boldsymbol{\rho}))\frac{\partial C(x, \boldsymbol{\rho})}{\partial x} = L_{\boldsymbol{\rho}} C(x, \boldsymbol{\rho}), \tag{2.19}$$

where

$$L_{\boldsymbol{\rho}} = \nabla_{\boldsymbol{\rho}} \cdot (\boldsymbol{D}_{\boldsymbol{\rho}} \nabla_{\boldsymbol{\rho}} - V_{c,\boldsymbol{\rho}}) \tag{2.20}$$

is the convection–diffusion operator in the transverse directions. The diffusion tensor $\boldsymbol{D}_{\boldsymbol{\rho}}$ and the mean velocity $V_{c,\boldsymbol{\rho}}$ in (2.20) contain only the elements corresponding to the transverse motion, i.e. for the 2-D flows, $V_{c,\boldsymbol{\rho}} = V_{c,y}$, $\boldsymbol{D}_{\boldsymbol{\rho}} = D_{yy}$ and for the 3-D flows,

$$V_{c,\boldsymbol{\rho}} = \begin{bmatrix} V_{c,y} \\ V_{c,z} \end{bmatrix}, \quad \boldsymbol{D}_{\boldsymbol{\rho}} = \begin{bmatrix} D_{yy} & D_{yz} \\ D_{yz} & D_{zz} \end{bmatrix}. \tag{2.21a,b}$$

The values of V_c and $\boldsymbol{D}$ were obtained from a series of Brownian dynamics simulations in a simple shear flow, which yield dependence of V_c and $\boldsymbol{D}$ on γ. To utilize these quantities in the mean-field model for a pressure-driven flow, the local shear $\gamma(\boldsymbol{\rho})$ in the flow is computed and spline interpolation of $V_c(\gamma)$ and $\boldsymbol{D}(\gamma)$ is performed to obtain their values corresponding to $\gamma(\boldsymbol{\rho})$. This yields velocities and diffusivities in a local system of coordinates $x\eta\zeta$ with the η and ζ axes pointing in the directions of $(0, \partial_y u_x^\infty, \partial_z u_x^\infty)$ and $(0, -\partial_z u_x^\infty, \partial_y u_x^\infty)$, respectively. The tensor $\boldsymbol{D}$ and the vector V_c are then rotated to obtain the diffusivity and the velocity in the directions of x, y and z.

Equation (2.19) was solved numerically using a finite-difference approximation for the operator $L_{\boldsymbol{\rho}}$ and the Runge–Kutta method for integration in the x direction. In addition, the developed profiles (corresponding to $\partial C/\partial x = 0$) were obtained directly by solving (2.19) with zero left-hand side. In the 2-D channel, this equation is solved analytically (see appendix B). In the 3-D channel, the developed profiles were obtained by numerically computing the eigenfunction corresponding to the zero eigenvalue of the operator $L_{\boldsymbol{\rho}}$.

3. Results

Results of Brownian dynamics simulations in a simple shear flow are presented in §§ 3.1 and 3.2, with comparisons between the long-range and short-range models for the electrohydrodynamic interactions. Then, results for pressure-driven flows are given in § 3.3, which include results of Brownian dynamics simulations and mean-field calculations. The shear rate is reported in terms of the Peclet number, i.e. dimensionless γ. Note that the Weissenberg number is given by 12γ (see § S2 of the supplementary material).
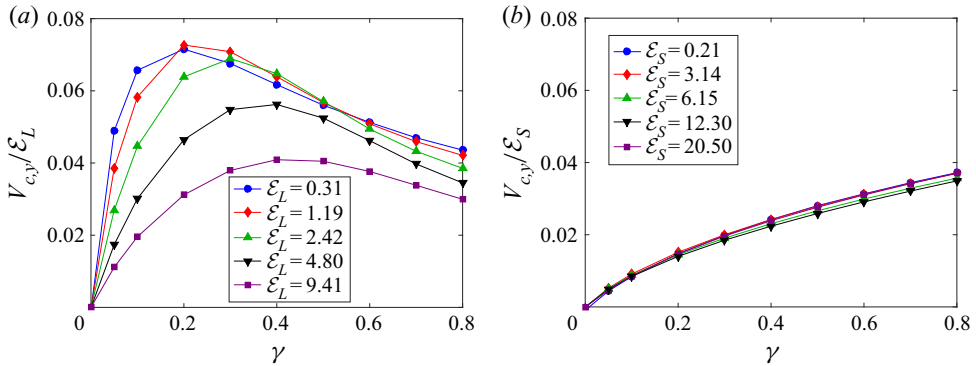
Figure 2. Mean transverse velocity $V_{c,y}$ in simple shear flows with rate γ. The results were obtained from Brownian dynamics simulations using (*a*) long-range and (*b*) short-range models for the electrohydrodynamic interactions. The velocities are normalized by the strength of the electric field $\mathcal{E}_m$ to facilitate discussion of the effects of $\mathcal{E}_m$ on $V_{c,y}$.

3.1. *Mean velocity in simple shear flow*

Dependence of the transverse velocity $V_{c,y}(\gamma, \mathcal{E}_m)$ of the polymer centre of mass in the simple shear flow on the shear rate γ is shown in figure 2 for several values of the electric field strength $\mathcal{E}_m$. Drift in the transverse direction is caused solely by electrohydrodynamic interactions. At zero shear rate, the polymer shape is nearly isotropic and the electrohydrodynamic interactions between polymer beads cancel out (see the discussion following (2.10)). Hence, $V_{c,y}(\gamma = 0; \mathcal{E}_m) = 0$ for all $\mathcal{E}_m$. Application of shear stretches and tilts the polymer with respect to the field direction, resulting in a non-zero electrohydrodynamic velocity $V_{c,y}$ in the transverse direction.

The long- and short-range electrohydrodynamic models predict qualitatively different dependence of $V_{c,y}$ on γ. The long-range model yields a non-monotonic dependence of $V_{c,y}$ on γ (see figure 2*a*): $V_{c,y}$ increases with γ for sufficiently small γ and decreases with further increase of γ, where both the maximum value and shear rate at which it occurs are functions of $\mathcal{E}_L$. In contrast, the short-range model predicts a monotonic increase of $V_{c,y}$ with γ (see figure 2*b*).

The qualitative differences observed in figure 2 cannot be attributed to changes in the structural properties of the polymer arising from the choice of electrohydrodynamic model. As shown in figure 3, the electrohydrodynamic model alters the structure quantitatively, but not qualitatively. Instead, the differences in $V_{c,y}$ arise from the dependencies of the electrohydrodynamic interactions on polymer stretching. As the polymer end-to-end distance increases in response to larger shear rates (see figure 3*a,b*), the magnitude of the electrohydrodynamic interactions can decrease or increase depending on which model is used.

Within the long-range model, $\hat{\mu}^E_{L,ij}(r)$ decreases as the distance r between beads increases (see (2.11)). This is consistent with the behaviour of $V_{c,y}$ obtained with the long-range model at high shear rates. The behaviour of $V_{c,y}$ at low shear rates is explained by the effect of the bond direction on electrohydrodynamic interactions. It follows from (2.9) and (2.10) that the velocity in the y direction induced by an electric field applied in the x direction is proportional to $\hat{r}_x\hat{r}_y$, where $\hat{r}$ is the normalized vector connecting pairs of polymer beads. On average, $\hat{r}_x\hat{r}_y$ can be characterized by the normalized covariance between the x and y components of the end-to-end vector $\boldsymbol{R}$ of the polymer,
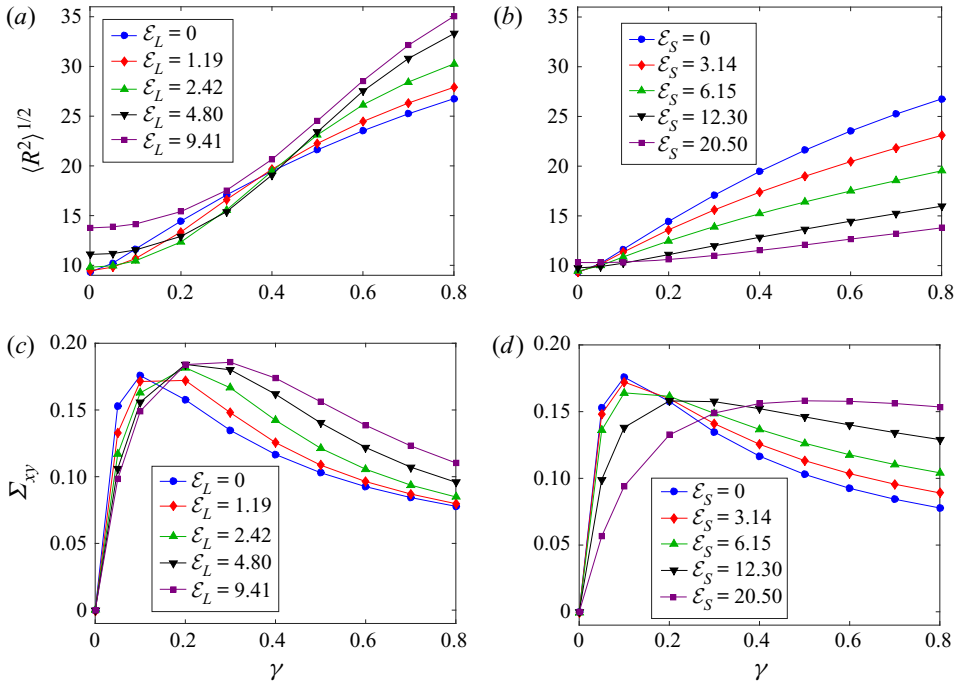
Figure 3. Structural properties of the polymer in a simple shear flow obtained from Brownian dynamics simulations. The root-mean-squared end-to-end distance $\langle R^2 \rangle^{1/2}$ is shown for the (*a*) long- and (*b*) short-range electrohydrodynamic models. The normalized covariance $\Sigma_{xy} = \langle R_x R_y \rangle / \langle R^2 \rangle$ of the x and y components of the end-to-end vector $\boldsymbol{R}$ are also shown for the (*c*) long- and (*d*) short-range models. Data are shown as a function of shear rate γ and electric field $\mathcal{E}_m$.

$\Sigma_{xy} = \langle R_x R_y \rangle / \langle R^2 \rangle$. This covariance, shown in figure 3(*c*,*d*), exhibits a non-monotonic dependence on γ. Therefore, at low shear rates, the decreasing trend of $\hat{\mu}^E_{L,ij}(r)$ competes with a very rapid increase of Σ_{xy}. Thus, $V_{c,y}$ obtained with the long-range model increases with γ at low shear rates.

Within the short-range model, $\hat{\mu}^E_{S,i,i\pm1}(r)$ increases as the distance r between beads increases (see (2.13*a*)), which is consistent with the observed dependence of $V_{c,y}$ on the shear rate (see figure 2*b*). At large γ, there is a competition between decreasing Σ_{xy} and increasing $\hat{\mu}^E_{S,i,i\pm1}(r)$. For the range of γ considered in the current work, the increase of $\hat{\mu}^E_{S,i,i\pm1}(r)$ is more substantial than the decrease of Σ_{xy} and, hence, the magnitude of $V_{c,y}$ grows with γ. The theoretical prediction of Ladd (2018) (which neglected the effect of the electrohydrodynamic interactions on the polymer configuration) shows that $V_{c,y}$ eventually reaches a maximum at large γ. However, this maximum is observed at a very high shear rate ($\gamma > 4$ in the current normalization), which is well beyond the values considered in the current simulations and the experiments of Arca *et al.* (2015). Moreover, this maximum is very weak, i.e. the rate of decrease of $V_{c,y}$ beyond this maximum is very small.

Figure 2 indicates that the transverse velocity depends on the field strength $\mathcal{E}_m$ as well as the shear rate. Since the magnitude of the instantaneous electrohydrodynamic velocity $\boldsymbol{v}^E_i$ of a bead is directly proportional to $\mathcal{E}_m$, it is expected that $V_{c,y}$ is also proportional to $\mathcal{E}_m$. This is indeed the case for the short-range model, as evident from figure 2(*b*). However, this is not always the case for the long-range model. The discrepancy is caused by changes in the polymer configuration induced by the electric field. For example, figure 3 shows
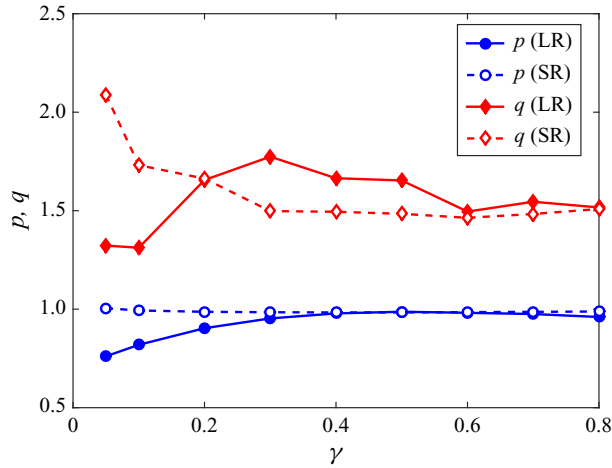
Figure 4. Power-law exponents p and q for the empirical relationships (3.1) and (3.2) describing the effect of the strength of the electric field $\mathcal{E}_m$ on the velocity $V_{c,y}$ and the diffusivity D_{yy} in the transverse direction predicted by the long-range (LR) and short-range (SR) electrohydrodynamic models.

that the root-mean-squared end-to-end distance $\langle R^2 \rangle^{1/2}$ and the normalized covariance Σ_{xy} of the end-to-end vector are affected by $\mathcal{E}_m$. Although the electric field also affects the polymer shape in the short-range model, its effect on $V_{c,y}$ is not as significant as in the long-range model. Despite the deviation from the linear dependence of $V_{c,y}$ on $\mathcal{E}_m$ in the long-range model, $V_{c,y}$ can be approximated by a power-law dependence on $\mathcal{E}_m$:

$$V_{c,y}(\gamma, \mathcal{E}_m) = \hat{V}_{c,y}(\gamma)\mathcal{E}_m^{p(\gamma)} \tag{3.1}$$

(see figure S4 in the supplementary material), with the exponent $p(\gamma)$ close to one. Dependence of the power-law exponent $p(\gamma)$ on the shear rate is shown in figure 4.

In addition to the qualitative difference in the mean drift velocities $V_{c,y}$, the long- and short-range models yield a substantial quantitative difference. Since the magnitudes of the parameters $\mathcal{E}_L$ and $\mathcal{E}_S$ corresponding to the same electric field strength E differ by three orders of magnitude for typical experimental conditions (see (2.15)) and the magnitudes of the normalized velocities $V_{c,y}/\mathcal{E}_m$ ($m = L$ or S) predicted by both electrohydrodynamic models are comparable (see figure 2), the values of velocities predicted by the long-range model are substantially smaller than those predicted by the short-range model at the same electric field and Debye length. To achieve the same transverse velocity at the same electric field in the long- and short-range models, it is necessary to increase the Debye length in the long-range model. This finding matches that of Ladd (2018).

3.2. *Diffusivity in simple shear flow*

The polymer diffusivity is also sensitive to $\mathcal{E}_m$, as shown in figure 5. This is explained by dispersion effects of electrohydrodynamic interactions: as the polymer configuration fluctuates, so do the electrohydrodynamic interactions between its beads. Therefore, in addition to the regular Brownian force due to thermal collisions between the polymer and the solvent, the random force acting on the polymer contains a contribution from the fluctuating component of electrohydrodynamic interactions. More specifically, the dynamics of internal degrees of freedom of the polymer contribute to translation of the polymer centre of mass. It is shown in § S3.3 of the supplementary material that the
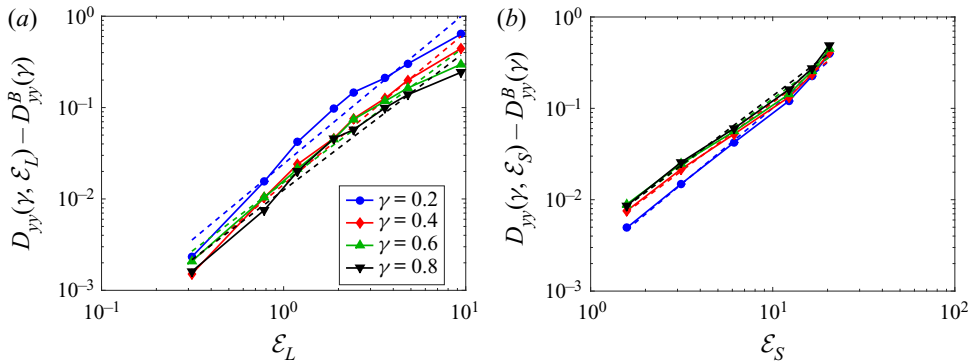
915 A59-12

Figure 5. Contribution of electrohydrodynamic dispersion to polymer diffusivity in the y direction in the simple shear flow obtained from Brownian dynamics simulations using (*a*) long-range and (*b*) short-range models. The dashed lines show fits of the data to the empirical relationship (3.2).

electrohydrodynamic dispersion is dominated by fast fluctuations of individual polymer beads. Contribution of slow fluctuations of the molecule as a whole (e.g. tumbling) is negligible in comparison with the fast fluctuations.

Fluctuations of electrohydrodynamic velocity increase in magnitude as the electric field becomes stronger. If the electric field were not to alter the polymer configuration, the instantaneous electrohydrodynamic force would be proportional to the field strength $\mathcal{E}_m$ and, hence, the contribution of this force to the diffusivity would scale as $\mathcal{E}_m^2$. However, as in the case with the mean drift velocity $V_{c,y}$, the polymer deformation caused by the electric field alters the value of the exponent. Therefore, the diffusivity is approximated by a more general expression:

$$D_{yy}(\gamma, \mathcal{E}_m) = D_{yy}^B(\gamma) + D_{yy}^E(\gamma)\mathcal{E}_m^{q(\gamma)}, \tag{3.2}$$

where $D_{yy}^B(\gamma) = D_{yy}(\gamma, 0)$ is the diffusivity due to the Brownian force and the second term of (3.2) represents the electrohydrodynamic dispersion. The Brownian diffusivity is obtained from simulations in the absence of an electric field and the characteristics of the electrohydrodynamic dispersion, D_{yy}^E and q, are obtained by fitting $[D_{yy}(\gamma, \mathcal{E}_m) - D_{yy}^B(\gamma)]$ to a power law, as shown in figure 5. Dependence of the power-law exponent $q(\gamma)$ on the shear rate γ is shown in figure 4. It is observed that $q(\gamma) > 1$ for all considered shear rates γ.

In addition to $V_{c,y}$ and D_{yy}, the mean-field model for the 3-D pressure-driven flow requires D_{zz} and D_{yz}. The component D_{zz} exhibits trends qualitatively similar to those of D_{yy} (see figure S5 in the supplementary material), with the power-law exponents q within the same range. The component D_{yz} is at least an order of magnitude smaller than D_{yy} and D_{zz} (see figure S3 in the supplementary material) and is therefore neglected in the mean-field analysis presented in § 3.3.

3.3. *Pressure-driven flows*

Brownian dynamics simulations of 2-D and 3-D pressure-driven flows were performed for a mean shear rate $\bar{\gamma} = 0.146$, which corresponds to the largest used in the experiments of Arca *et al.* (2015). Typical evolution of the concentration profile in the 2-D flow is shown in figure 6. It is observed that the distribution of the polyelectrolyte narrows downstream of the channel entrance at $x = 0$, where the distribution was uniform. The concentration
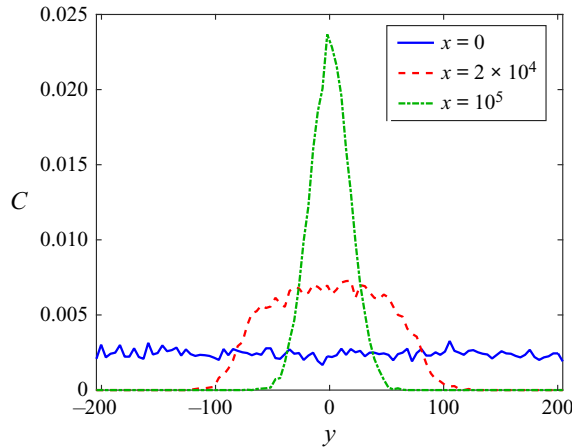
Figure 6. Concentration profiles in a 2-D pressure-driven flow at various positions x along the channel obtained by the Brownian dynamics simulations with uniform initial conditions. The results were generated using the long-range model with $\mathcal{E}_L = 9.41$ and $\bar{\gamma} = 0.146$. Positions $x \geq 10^5$ correspond to the fully developed profile. The profiles are normalized so that $\int C(y)\,\mathrm{d}y = 1$.
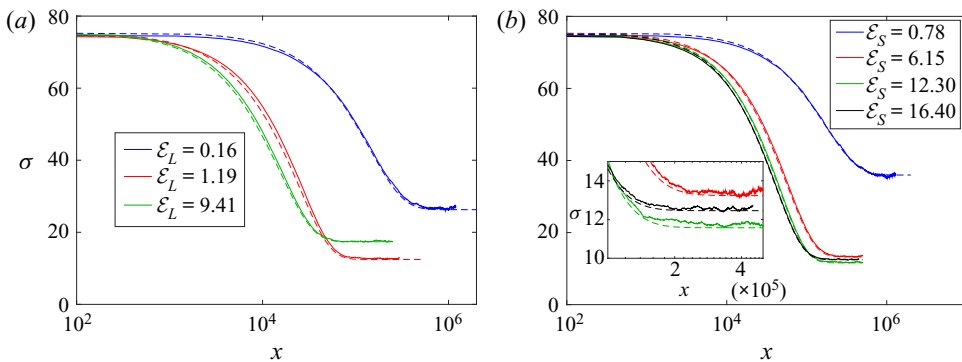

Figure 7. Dependence of widths σ of the concentration profiles on position x along the channel in 2-D pressure-driven flows. The data were obtained by the Brownian dynamics simulations (solid lines) and the mean-field model (dashed lines) at $\bar{\gamma} = 0.146$ using (*a*) long-range and (*b*) short-range approximations. The inset in (*b*) shows a magnified area corresponding to developed profiles for $\mathcal{E}_S = 6.15$, 12.30 and 16.40.

profile eventually becomes independent of the position x along the channel, and this fully developed concentration profile is independent of the initial conditions as shown in figures S9–S11 in the supplementary material. Therefore, unless stated otherwise, we focus on results obtained with the initial conditions determined from the experimental data (see § S4.1 in the supplementary material) which are not quite uniform at $x = 0$.

Evolution of the concentration profile width σ (see figure 1*a* for definition) along the channel length is shown in figure 7 for 2-D flows; similar results were obtained for 3-D flows, as shown in figure S12 in the supplementary material. Results, shown for a range of electric fields with a fixed flow rate (mean shear), indicate that the distribution moves towards its developed value more rapidly with increasing electric field.

To further facilitate analysis of pressure-driven flows, we utilize the mean-field model described in § 2.5. One of the main assumptions of this model is that the polymer adjusts to its local environment (determined by a local shear rate) much faster than it travels
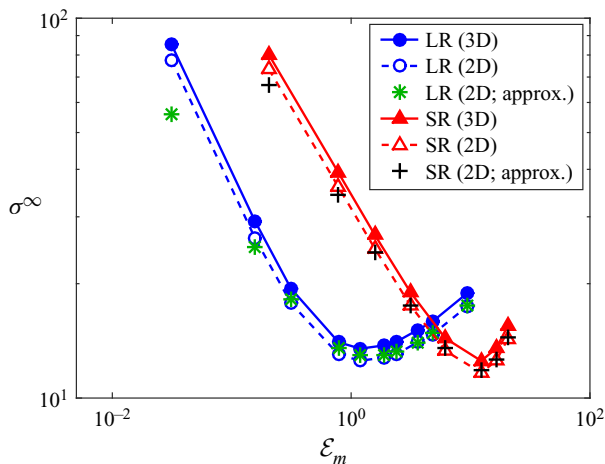
Figure 8. Widths (σ^∞) of the developed profiles in 2-D and 3-D pressure-driven flows with mean shear rate $\bar\gamma = 0.146$ in channels of width $H = 413$ obtained using the mean-field model for the long-range (LR) and short-range (SR) approximations of the electrohydrodynamic interactions. The asterisks and crosses indicate the approximate solutions (3.9) of the 2-D mean-field model.

in the transverse direction. This enables us to use the values of the velocity V_c and the diffusivity D determined from the Brownian dynamics simulations in simple shear flows. This assumption is validated by an order-of-magnitude estimation of the relevant time scales presented in § S4.3.1 of the supplementary material. In addition, the validity of the mean-field model is confirmed by a direct comparison of its predictions with the Brownian dynamics simulations. As shown in figure 7, results of the mean-field model (shown by the dashed lines) and the Brownian dynamics (solid lines) are in excellent agreement for the 2-D pressure-driven flow; the mean-field model accurately predicts not only the developed profiles, but also the transient states. Similarly good agreement between the mean-field model and the Brownian dynamics simulations is observed for the 3-D pressure-driven flow (see figure S14 in the supplementary material). In § S4.4 of the supplementary material we utilize the mean-field model to investigate developing concentration profiles and assess effects of the electric field strength and the mean shear rate on the entrance length required to reach a developed profile. In the remainder of this section, we apply the mean-field model to analyse well-developed profiles.

Figure 7 indicates that the width σ^∞ (σ as $x \to \infty$) of the fully developed profile is a non-monotonic function of the electric field $\mathcal{E}_m$ for both models of electrohydrodynamic interactions. This non-monotonic dependence is shown more clearly in figure 8 using data from the mean-field calculations. The difference between σ^∞ in the 2-D and 3-D flows is small, with the 3-D flow producing slightly wider concentration profiles than the 2-D flow at the same $\mathcal{E}_m$ and $\bar\gamma$. The similarity between the 2-D and 3-D flows is also observed during the development stage of the profiles (see figure S12 in the supplementary material). In particular, the rate of convergence towards a developed profile is almost the same in 2-D and 3-D geometries at identical $\mathcal{E}_m$ and $\bar\gamma$.

Since the 2-D and 3-D pressure-driven flows yield similar results, the remainder of this paper focuses on analysis of the 2-D flow. The 2-D flow velocity profile and the local shear

rate corresponding to the mean shear rate of $\bar{\gamma}$ are

$$u_x^\infty(y) = \frac{2\bar{\gamma}}{H}\left[\left(\frac{H}{2}\right)^2 - y^2\right] \tag{3.3}$$

and

$$\gamma(y) = -\frac{4\bar{\gamma}y}{H}, \tag{3.4}$$

respectively (the system of coordinates is chosen so that $y = 0$ corresponds to the centre of the channel). As shown in appendix B, the developed concentration profile in a 2-D channel is

$$C(y;\mathcal{E}_m) \propto \exp\left[\int_0^y R(\gamma(y');\mathcal{E}_m)\,\mathrm{d}y'\right], \tag{3.5}$$

where

$$R(\gamma;\mathcal{E}_m) = \frac{V_{c,y}(\gamma;\mathcal{E}_m)}{D_{yy}(\gamma;\mathcal{E}_m)} \tag{3.6}$$

is the ratio of the transverse velocity and diffusivity.

The electrohydrodynamic drift vanishes in the absence of shear, $V_{c,y}(\gamma = 0) = 0$. Therefore, to leading order,

$$R(\gamma;\mathcal{E}_m) \approx c(\mathcal{E}_m)\gamma \tag{3.7}$$

for small γ. The function c depends only on the type of the electrohydrodynamic model and the strength $\mathcal{E}_m$ of the electric field. Substituting (3.4) and (3.7) into (3.5), we obtain

$$C(y;\mathcal{E}_m) \propto \exp\left[\int_0^y c(\mathcal{E}_m)\gamma(y')\,\mathrm{d}y'\right] = \exp\left[-\frac{2c(\mathcal{E}_m)\bar{\gamma}}{H}y^2\right]. \tag{3.8}$$

Hence, the developed concentration profile can be approximated by a Gaussian distribution with the standard deviation

$$\sigma^\infty(\bar{\gamma};\mathcal{E}_m) = \frac{1}{2}\left[\frac{H}{c(\mathcal{E}_m)\bar{\gamma}}\right]^{1/2}. \tag{3.9}$$

As shown in figure 8, this approximation is in good agreement with the solution of the full 2-D mean-field equation (B1) for most of the considered conditions. The only exception is the profile at the lowest considered electric field strength ($\mathcal{E}_L = 0.03$) in the long-range model. The discrepancy is caused by an inaccuracy of the linear approximation (3.7) inside this wide profile: the local shear rate at distance $\sigma^\infty(\mathcal{E}_L = 0.03) \approx 80$ from the channel centre is $\gamma \approx 0.1$. It is clear from figure 9(*a*) that dependence of $R(\gamma;\mathcal{E}_L \leq 0.31)$ deviates from the linear behaviour for $0 \leq \gamma \leq 0.1$, which explains the discrepancy between the approximate and full solution of the mean-field model. Note that the approximation (3.9) works much better for a concentration profile of comparable width obtained with the short-range model (at $\mathcal{E}_S = 0.21$). This good agreement is due to the fact that $R(\gamma;\mathcal{E}_S = 0.21)$ exhibits a linear dependence on γ for a wide range of γ (see figure 9*b*).
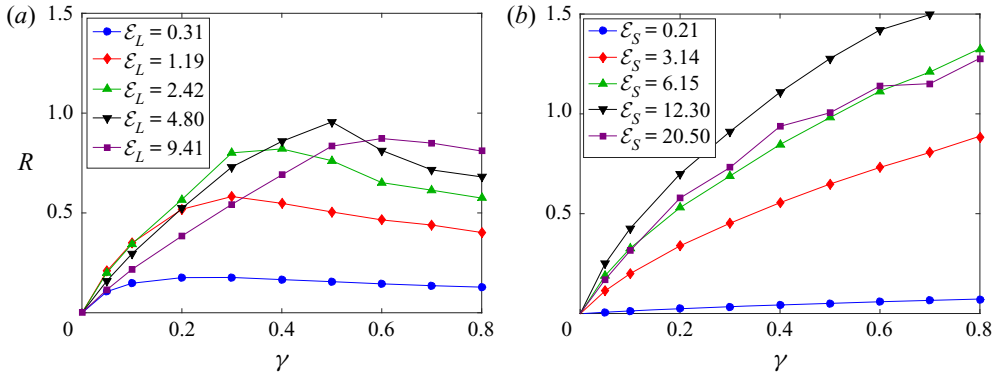
Figure 9. Ratio $R = V_{c,y}/D_{yy}$ of the transverse velocity and diffusivity in a simple shear flow. The ratio R was obtained from the Brownian dynamics simulations using (*a*) long-range and (*b*) short-range models.

4. Discussion

4.1. *Dependence of the profile width on the mean shear rate*

The approximate expression (3.9) for the developed profile width σ^∞ indicates that $\sigma^\infty \propto \bar{\gamma}^{-1/2}$. This scaling is consistent with the experimental observations of Arca *et al.* (2015) (see figure 1*b*). This scaling was also obtained analytically for a dumbbell polyelectrolyte model with the long-range (Butler *et al.* 2007) and short-range (Setaro & Underhill 2019) approximations of the electrohydrodynamic interactions. The current work demonstrates that the scaling holds for more general multi-bead polymer models. Since the approximation (3.9) is based on the leading-order term of the Taylor series expansion of the ratio $R = V_{c,y}/D_{yy}$ (see (3.7)), the scaling $\sigma^\infty \propto \bar{\gamma}^{-1/2}$ does not depend on details of the electrohydrodynamic model, as long as $\bar{\gamma}$ is sufficiently small.

Furthermore, this scaling may hold even at a relatively large mean shear rate $\bar{\gamma}$, provided that the ratio of the transverse velocity and diffusivity remains proportional to the shear rate (3.7) within the fully developed flow. This condition is satisfied if the developed concentration profile is sufficiently narrow (i.e. the polymers are concentrated in the low-shear region) and/or the linear approximation (3.7) is valid for a wide range of γ. Figure 9 indicates that the latter condition is satisfied for the short-range model, whereas the long-range model exhibits a strongly nonlinear (non-monotonic) dependence of the ratio R on γ. Therefore, it is expected that, within the short-range model, the $\bar{\gamma}^{-1/2}$ scaling of σ^∞ holds even for wide concentration profiles and large shear rates. On the other hand, the long-range model is expected to yield this scaling only for small shear rates and/or sufficiently large electric field strength (since the latter produces a strong focusing of the polyelectrolyte).

This is confirmed by figure 10, which shows $\sigma^\infty(\bar{\gamma})$ obtained by solving the full mean-field equation (B1) for the 2-D pressure-driven flow. For the short-range model, the scaling $\sigma^\infty \propto \bar{\gamma}^{-1/2}$ holds even for relatively wide concentration profiles (observed at a low electric field strength). In contrast, in the long-range model, this scaling holds only for relatively narrow concentration profiles. At a weak electric field, the long-range model predicts the $\bar{\gamma}^{-1/2}$ scaling only for very small $\bar{\gamma}$. However, at a moderate electric field strength, the concentration profile is sufficiently narrow so that the $\bar{\gamma}^{-1/2}$ scaling holds at relatively large $\bar{\gamma}$ even with the long-range model.
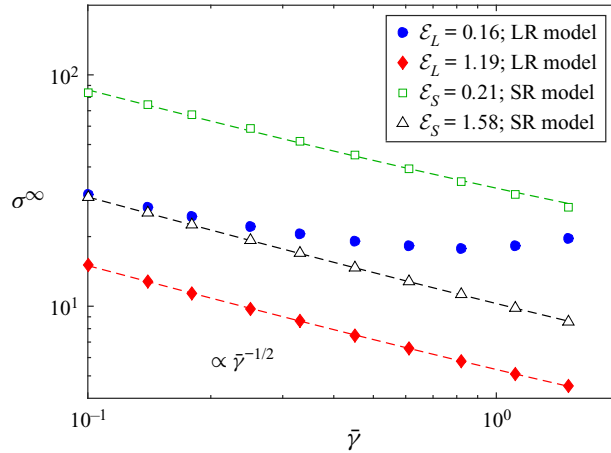
Figure 10. Effect of the mean shear rate $\bar{\gamma}$ on the width σ^{∞} of the developed concentration profile in a 2-D pressure-driven flow predicted by the mean-field model for the long-range (LR) and short-range (SR) approximations of the electrohydrodynamic interactions. The dashed lines show results of a fit of $\sigma^{\infty}(\bar{\gamma})$ to $\sigma_0 \bar{\gamma}^{-1/2}$ (σ_0 is a constant).

4.2. *Dependence of the profile width on the electric field strength*

As shown in figure 8, both the long- and short-range models predict the existence of an optimal field strength $\mathcal{E}_m^*$ leading to the narrowest concentration profile. This is in qualitative agreement with experimental observations of Arca *et al.* (2015) (see figure 1*b*), previous simulations of the long-range model (Kekre *et al.* 2010*b*) and analysis of the short-range model for a dumbbell approximation to a polymer (Setaro & Underhill 2019). Here, we explain the mechanism leading to existence of the optimal field strength.

Equation (3.9) indicates that the optimal field $\mathcal{E}_m^*$ corresponds to the maximum of $c(\mathcal{E}_m) = \partial R(\gamma; \mathcal{E}_m)/\partial \gamma|_{\gamma=0}$. Therefore, at small shear rates γ, $\mathcal{E}_m^*$ corresponds to the maximum of the ratio $R(\gamma; \mathcal{E}_m)$ of the drift velocity and diffusivity in the transverse direction. This maximum arises due to an interplay between the Brownian motion and the electrohydrodynamic drift and dispersion. To see this, consider the inverse of R and use the empirical relationships (3.1) and (3.2) for $V_{c,y}$ and D_{yy}:

$$R^{-1}(\gamma; \mathcal{E}_m) = \frac{D_{yy}(\gamma; \mathcal{E}_m)}{V_{c,y}(\gamma; \mathcal{E}_m)} = \frac{D_{yy}^B(\gamma)}{\hat{V}_{c,y}(\gamma)} \mathcal{E}_m^{-p} + \frac{D_{yy}^E(\gamma)}{\hat{V}_{c,y}(\gamma)} \mathcal{E}_m^{q-p}. \quad (4.1)$$

Since $q > p > 0$ (see figure 4), the first and second terms of (4.1) are monotonically decreasing and increasing functions, respectively. Therefore, the sum of these functions has a single minimum corresponding to the optimal electric field strength $\mathcal{E}_m^*$, as illustrated in figure 11. This result holds for both considered models because in both cases the electrohydrodynamic velocity is approximately proportional to the electric field ($p \approx 1$) and the electrohydrodynamic dispersion scales as $\mathcal{E}_m^q$ with $q > 1$. These scalings are expected to be quite general, since the mean and variance of the electrohydrodynamic velocity are expected to be proportional to $\mathcal{E}_m$ and $\mathcal{E}_m^2$, respectively. The discrepancy between these expected scalings and those observed in the Brownian dynamics simulations is due to polymer deformation caused by the electrohydrodynamic interactions.

Although $\sigma^{\infty}(\mathcal{E}_m)$ predicted by both models is in qualitative agreement with the experiment of Arca *et al.* (2015), there is a substantial quantitative difference between the model predictions and the experimental data, as summarized in table 2. The values of
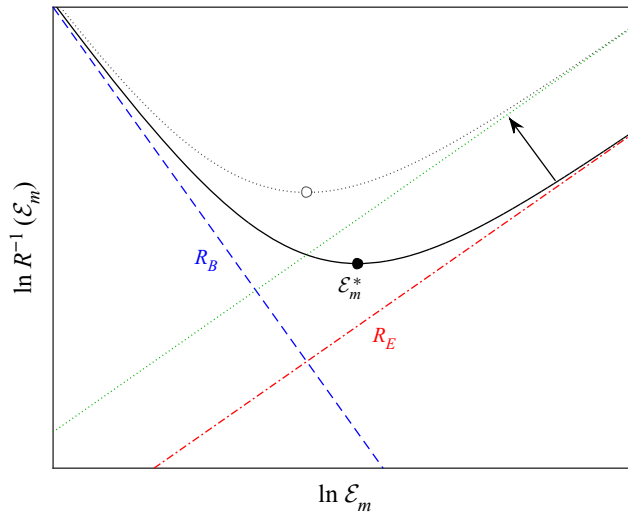
Figure 11. Schematic of contributions of individual terms of (4.1) to R^{-1}. The contributions of the Brownian force ($R_B = (D_{yy}^B/\hat{V}_{c,y})\mathcal{E}_m^{-p}$) and the electrohydrodynamic dispersion ($R_E = (D_{yy}^E/\hat{V}_{c,y})\mathcal{E}_m^{q-p}$) are shown by the blue dashed and red dash-dotted lines, respectively. The solid black line is R^{-1} and the optimal electric field $\mathcal{E}_m^*$ is shown by the filled circle. The dotted lines show the effect of increasing the magnitude of the electrohydrodynamic dispersion relative to the electrohydrodynamic drift (the green and black dotted lines show new R_E and R^{-1}, respectively, and the open circle shows new $\mathcal{E}_m^*$).

λ_D	E_{exp}^*	α_μ	E_L^*	E_S^*
0.019	0.14	0.52	4.3	0.43
0.120	0.02	0.55	0.1	0.48

Table 2. Comparison of the optimal electric fields obtained from experiment (Arca *et al.* 2015) and the combination of the Brownian dynamics simulations with the mean-field analysis. Here E_{exp}^*, E_L^* and E_S^* denote the optimal electric fields obtained, respectively, from the experiment and the analysis with the long- and short-range models. The electric field is normalized by the characteristic electric field $k_B T/be = 1305$ V cm^{-1}.

the predicted optimal electric fields E_m^* ($m = L$ and S) reported in this table are computed from the optimal values of $\mathcal{E}_m$ ($\mathcal{E}_L^* = 1.19$ and $\mathcal{E}_S^* = 12.30$) using (2.12) and (2.14) for the Debye lengths λ_D used in the experiment. The ratio α_μ of the parallel and perpendicular components of the electrohydrodynamic rod mobility tensor (needed to compute E_S^* from $\mathcal{E}_S^*$) is obtained using the slender body model (Chen & Koch 1996) approximating a single Kuhn step as a cylinder of diameter 1 nm and length 106 nm.

Both considered models for electrohydrodynamic interactions overestimate the magnitude of the optimal electric field E^*. Moreover, scaling of E^* with λ_D suggested by the experimental data ($E^* \propto \lambda_D^{-1}$) is different from that predicted by the models. According to the long-range model, $E^* \propto \lambda_D^{-2}$ (see (2.12)) and the short-range model predicts a very weak dependence of α_μ on λ_D, with α_μ varying between 0.5 and 0.6 for the range of experimental values of λ_D. Hence, according to the short-range model, changing the Debye length should have a small effect on the optimal electric field E^*, which contradicts the experimental results.

In addition to overestimating the magnitude of the optimal electric field $\mathcal{E}_m^*$, the considered electrohydrodynamic interaction models underestimate the width $\sigma^\infty(\mathcal{E}_m^*)$ of the narrowest concentration profile. Both models yield $\sigma^\infty(\mathcal{E}_m^*) \approx 13$ at $\bar{\gamma} = 0.146$ in the 3-D channel (see figure 8), whereas the experimental value for these conditions is $\sigma^\infty(\mathcal{E}_m^*) \approx 20$ (see figure 1). Therefore, to improve agreement with the experiment, an improved model for electrohydrodynamic interactions should yield a smaller $\mathcal{E}_m^*$ and a larger $\sigma^\infty(\mathcal{E}_m^*)$. As illustrated in figure 11, this can be accomplished by increasing $R_E \equiv (D_{yy}^E/\hat{V}_{c,y})\mathcal{E}_m^{q-p}$, i.e. the magnitude of the electrohydrodynamic dispersion relative to the magnitude of the electrohydrodynamic drift.

5. Conclusions

The Brownian dynamics simulations and the mean-field analysis performed in the current study elucidated mechanisms of two electrohydrodynamic phenomena observed in earlier experimental (Arca *et al.* 2015) and computational and analytical (Kekre *et al.* 2010*b*; Setaro & Underhill 2019) studies of pressure-driven flows of polyelectrolytes in microfluidic channels. Specifically, the current work confirms and explains the scaling of the width σ^∞ of the fully developed concentration profile with the mean shear rate $\bar{\gamma}$, $\sigma^\infty \propto \bar{\gamma}^{-1/2}$. It is demonstrated that this scaling holds for both the long- and short-range approximations of electrohydrodynamic interactions. However, the long-range model produces the scaling only at small shear rates and/or sufficiently strong electric fields, whereas the short-range model does not require these additional restrictions.

Furthermore, the current work explains the observed dependence of the profile width σ^∞ on the electric field E. Specifically, it is shown that the non-monotonic dependence of σ^∞ on E is caused by dispersion created by fluctuations of electrohydrodynamic interactions within a polymer. The specific value of E^* is determined by a balance between the Brownian diffusion and the electrohydrodynamic drift and dispersion (see figure 11). The optimal electric field E^* is observed with both the short- and long-range electrohydrodynamic models considered in the current work, in qualitative agreement with the experiment. In addition, the mechanism is expected to be general and hold for any future refinements of the electrohydrodynamic models.

That these refinements are necessary is indicated by the quantitative discrepancy between the predicted and experimental values of E^*. Both the long- and short-range models overestimate E^* and underestimate the profile width $\sigma^\infty(E^*)$ at this E^*. As discussed in § 4.2, this indicates that these models underestimate the ratio of the electrohydrodynamic dispersion and drift. An improved model should contain features of both the long- and short-range models, i.e. it should contain electrohydrodynamic interactions between different groups of a polymer (as in the long-range model) as well as mobility of individual Kuhn steps of the polymer chain (as in the short-range model). This model should also account for medium-range electrohydrodynamic interactions between the Kuhn steps (Ladd 2018), which were neglected in the current work. Since each of these factors contributes to electrohydrodynamic dispersion, a model combining them is expected to yield a larger total dispersion. The medium-range model requires development of an accurate model for electrohydrodynamic interactions between rods, which can be accomplished by extending the slender body model of Chen & Koch (1996). The rod interaction model can then be validated by experiments on electrophoresis of non-dilute rigid segments of polyelectrolyte.

In addition, dispersion is expected to be sensitive to the number of beads in the bead–spring model and one needs to select an appropriate level of discretization when

approximating electrohydrodynamic interactions in the polymer. This, together with a model combining long-, medium- and short-range interactions will be explored in future work.

Author ORCIDs.

- Dmitry I. Kopelevich https://orcid.org/0000-0001-9674-3551;
- Shujun He https://orcid.org/0000-0003-1010-536X;
- Ryan J. Montes https://orcid.org/0000-0003-4197-4736;
- Jason E. Butler https://orcid.org/0000-0003-2513-9116.

Appendix A. Details of electrohydrodynamic models

This appendix reviews the derivation of the long- and short-range models, demonstrates that both of these models can be written as (2.9) and obtains the expressions for parameters $\mathcal{E}_m$ and functions $\hat{\mu}^E_{m,ij}$ characterizing electrohydrodynamic interactions.

A.1. *Long-range model*

Within the framework of this model (Butler *et al.* 2007; Kekre *et al.* 2010*b*), each bead of the polymer chain is assumed to be a sphere containing uniformly distributed point charges. The electrohydrodynamic flow at the centre of mass of the ith bead generated by charges contained in the jth bead is approximated by the leading term of a multi-pole expansion:

$$\boldsymbol{v}^E_{ij} = \int_{|\boldsymbol{r}-\boldsymbol{r}_j|\leq a} \rho_Q(\boldsymbol{r})\boldsymbol{v}^{E,point}(\boldsymbol{r}-\boldsymbol{r}_i)\,\mathrm{d}\boldsymbol{r} \approx Q\boldsymbol{v}^{E,point}(\boldsymbol{r}_j-\boldsymbol{r}_i). \tag{A1}$$

Here, $\rho_Q(\boldsymbol{r})$ is the charge density of the bead centred at $\boldsymbol{r}=\boldsymbol{r}_j$, Q is the total charge of the bead and $\boldsymbol{v}^{E,point}(\boldsymbol{r})$ is the electrohydrodynamic flow field at point $\boldsymbol{r}$ generated by a point charge of unit magnitude located at the origin and its surrounding counterion cloud (Allison & Stigter 2000; Long & Ajdari 2001):

$$\boldsymbol{v}^{E,point}(\boldsymbol{r}) = \frac{\lambda_D^2}{4\pi\eta r^3}\boldsymbol{A}(\hat{\boldsymbol{r}})E. \tag{A2}$$

Here, λ_D is the Debye length, $\hat{\boldsymbol{r}}=\boldsymbol{r}/r$ and tensor $\boldsymbol{A}(\hat{\boldsymbol{r}})$ is defined by (2.10). In writing (A2), we neglected the exponentially decaying terms proportional to $\exp(-r/\lambda_D)$ because the distance r between beads typically exceeds multiple Kuhn lengths $l_K = O(100\text{ nm})$ and, hence, is significantly larger than the Debye length $\lambda_D \leq O(10\text{ nm})$. Furthermore, electrohydrodynamic interactions between overlapping beads are neglected. Therefore, the electrohydrodynamic velocity of the ith bead can be written as (2.9) with $\hat{\mu}^E_{L,ij}(r)$ and $\mathcal{E}_L$ given by (2.11) and (2.12), respectively.

A.2. *Short-range model*

This model (Liao *et al.* 2010; Pandey & Underhill 2015; Ladd 2018) represents a DNA molecule as a chain of rigid rods (Kuhn steps) of length l_K. Response of each of the rods

to the electric field is described by the mobility tensor

$$\boldsymbol{\mu}^{E,rod}(\boldsymbol{p}) = \mu_\parallel^{E,rod}\boldsymbol{pp} + \mu_\perp^{E,rod}(\boldsymbol{I} - \boldsymbol{pp}), \tag{A3}$$

where $\boldsymbol{p}$ is the rod director of unit length. This tensor contains contributions of both the electrophoretic mobility and the electrohydrodynamic interactions.

The entire polymer chain is split into subchains of equal contour length. Each subchain corresponds to a chain connecting neighbouring beads in the bead–spring model. The mobility tensor $\boldsymbol{\mu}^{E,chain}$ describing response of a subchain to an electric field is obtained by averaging over orientations of rods comprising it. In the current work, we use the Kirkwood–Riseman averaging (Kirkwood & Riseman 1948), which assumes that the subchain mobility is the mean of mobilities of individual rods, i.e.

$$\boldsymbol{\mu}^{E,chain} = \langle \boldsymbol{\mu}^{E,rod} \rangle. \tag{A4}$$

Assuming, furthermore, that the rods form a freely jointed chain, the mobility of a subchain connecting beads i and j ($j = i \pm 1$) is (Ladd 2018)

$$\boldsymbol{\mu}^{E,chain}(\boldsymbol{r}_{ij}) = \mu_\parallel^{E,chain}\hat{\boldsymbol{r}}_{ij}\hat{\boldsymbol{r}}_{ij} + \mu_\perp^{E,chain}(\boldsymbol{I} - \hat{\boldsymbol{r}}_{ij}\hat{\boldsymbol{r}}_{ij}), \tag{A5}$$

with

$$\mu_\parallel^{E,chain}(n_{ij}) = \mu_\parallel^{E,rod}\left(1 - \frac{2n_{ij}}{L^{-1}(n_{ij})}\right) + 2\mu_\perp^{E,rod}\frac{n_{ij}}{L^{-1}(n_{ij})}, \tag{A6}$$

$$\mu_\perp^{E,chain}(n_{ij}) = \mu_\parallel^{E,rod}\frac{n_{ij}}{L^{-1}(n_{ij})} + \mu_\perp^{E,rod}\left(1 - \frac{n_{ij}}{L^{-1}(n_{ij})}\right). \tag{A7}$$

Here, $n_{ij} = r_{ij}/r_0$ and $L^{-1}(n_{ij})$ is the inverse Langevin function representing the normalized tension in the freely jointed chain. Rearranging (A5), (A6) and (A7), we obtain

$$\boldsymbol{\mu}^{E,chain}(\boldsymbol{r}_{ij}) = \mu_0^E\boldsymbol{I} + \tfrac{1}{3}(\mu_\parallel^{E,rod} - \mu_\perp^{E,rod})\hat{\mu}^{E,chain}(\boldsymbol{r}_{ij})\boldsymbol{A}(\hat{\boldsymbol{r}}_{ij}), \tag{A8}$$

where $\mu_0^E = (\mu_\parallel^{E,rod} + 2\mu_\perp^{E,rod})/3$ is the overall rod mobility, the tensor $\boldsymbol{A}(\hat{\boldsymbol{r}}_{ij})$ is defined by (2.10) and

$$\hat{\mu}^{E,chain}(\boldsymbol{r}_{ij}) = 1 - \frac{3n_{ij}}{L^{-1}(n_{ij})} = \frac{2n_{ij}^2}{3 - n_{ij}^2}. \tag{A9}$$

The second equality in (A9) is obtained using the Padé approximation (Cohen 1991) to L^{-1}:

$$L^{-1}(n) = n\frac{3 - n^2}{1 - n^2}. \tag{A10}$$

It is convenient to express the magnitude of electrohydrodynamic interactions in terms of the ratio $\alpha_\mu = \mu_\perp^{E,rod}/\mu_\parallel^{E,rod}$ of the components of the rod mobility tensor:

$$\frac{1}{3}\left(\mu_\parallel^{E,rod} - \mu_\perp^{E,rod}\right) = \frac{1 - \alpha_\mu}{1 + 2\alpha_\mu}\mu_0^E. \tag{A11}$$

To implement the short-range model in the Brownian dynamics simulations of the bead–spring model, it is necessary to convert the electrohydrodynamic mobility of a subchain to that of a bead. Following Liao *et al.* (2010) and Pandey & Underhill (2015), the

915 A59-22

bead mobility is taken to be the average of mobilities of subchains adjacent to the bead. It then follows that the electrohydrodynamic velocity of a bead within the short-range model is given by (2.9) with the strength of electrohydrodynamic interactions characterized by the function $\hat{\mu}_{S,i,i\pm1}^{E}$ and the parameter $\mathcal{E}_S$ given by (2.13a) and (2.14), respectively.

Equations (A8) and (A9) indicate that stretching a subchain increases its electrohydrodynamic mobility and the mobility of a fully stretched subchain ($n_{ij} = 1$) coincides with that of a single rod. The mobility of a partially stretched chain is smaller than that of a fully stretched chain because of partial cancellation of mobilities of non-parallel rods (contained within a partially stretched chain) during averaging. This feature of the short-range model is expected to be independent of specific method of averaging of $\mu^{E,rod}$ employed to obtain $\mu^{E,chain}$.

In fact, earlier simulations employing the short-range model (Liao *et al.* 2010; Pandey & Underhill 2015) utilized an alternative averaging method to obtain $\mu^{E,chain}$. Specifically, Zimm averaging (Zimm 1980) was performed. Within this approach, a subchain is assumed to be a rigid object so that

$$\mu^{H,chain}\mu^{E,chain} = \langle\mu^{H,rod}\mu^{E,rod}\rangle, \tag{A12}$$

where $\mu^{H,chain}$ and $\mu^{H,rod}$ are hydrodynamic friction tensors of a subchain and a rod, respectively. It was shown by Ladd (2018) that the Zimm and Kirkwood–Riseman approximations yield very similar numerical values for the subchain mobilities. Therefore, it is expected that the specific choice of the averaging approximation does not have a significant effect on simulation results. Furthermore, the Zimm averaging performed by Pandey & Underhill (2015) assumed that the rod hydrodynamic friction tensor $\mu^{H,rod}$ is isotropic. With this choice, $\mu^{H,chain} = \mu^{H,rod}$ and Zimm averaging reduces to the Kirkwood–Riseman averaging. Therefore, the model employed in the current work is equivalent to that of Pandey & Underhill (2015).

Appendix B. Analytical solution for the developed concentration profile in a 2-D channel

A developed concentration profile in a 2-D channel satisfies the following one-dimensional convection–diffusion equation:

$$\frac{d}{dy}\left[D_{yy}(y)\frac{dC}{dy} - V_{c,y}(y)C\right] = 0. \tag{B1}$$

We consider a channel of width H centred at $y = 0$. The polymer concentration is assumed to be symmetric with respect to the channel centre, i.e.

$$\frac{dC(y)}{dy} = 0 \quad \text{at } y = 0. \tag{B2}$$

In addition, the shear rate at the centre of the channel is zero and, hence, the electrohydrodynamic drift is also zero:

$$V_{c,y}(0) = 0. \tag{B3}$$

Integrating (B1), we obtain

$$D_{yy}(y)\frac{dC}{dy} - V_{c,y}(y)C = A, \tag{B4}$$

where $A = $ const. It follows from (B2) and (B3) that the left-hand side of (B4) is zero at $y = 0$. Hence, $A = 0$ and the solution of (B4) is

$$C(y) = B \exp\left[\int_0^y \frac{V_{c,y}(y')}{D_{yy}(y')}\, \mathrm{d}y'\right].$$ (B5)

The constant B is obtained from a normalization condition. In the current work, we normalize $C(y)$ so that it represents the probability density of the polymers, i.e. $\int_{-H/2}^{H/2} C(y)\, \mathrm{d}y = 1$.

REFERENCES

ALLISON, S.A. & STIGTER, D. 2000 A commentary on the screened-Oseen, counterion-condensation formalism of polyion electrophoresis. *Biophys. J.* **78**, 121–124.

ARCA, M., BUTLER, J.E. & LADD, A.J.C. 2015 Transverse migration of polyelectrolytes in microfluidic channels induced by combined shear and electric fields. *Soft Matt.* **11** (22), 4375–4382.

ARCA, M., LADD, A.J.C. & BUTLER, J.E. 2016 Electro-hydrodynamic concentration of genomic length DNA. *Soft Matt.* **12**, 6975–6984.

BUTLER, J.E., USTA, O.B., KEKRE, R. & LADD, A.J.C. 2007 Kinetic theory of a confined polymer driven by an external force and pressure-driven flow. *Phys. Fluids* **19**, 113101.

CHEN, S.B. & KOCH, D.L. 1996 Electrophoresis and sedimentation of charged fibers. *J. Colloid Interface Sci.* **180**, 466–477.

COHEN, A. 1991 A Padé approximant to the inverse Langevin function. *Rheol. Acta* **30**, 270–273.

ERMAK, D.L. & MCCAMMON, J.A. 1978 Brownian dynamics with hydrodynamic interactions. *J. Chem. Phys.* **69**, 1352–1360.

KEKRE, R., BUTLER, J.E. & LADD, A.J.C. 2010a Comparison of Boltzmann and Brownian Dynamics simulations of polymer migration in confined flows. *Phys. Rev.* E **82**, 011802.

KEKRE, R., BUTLER, J.E. & LADD, A.J.C. 2010b Role of hydrodynamic interactions in the migration of polyelectrolytes driven by a pressure gradient and an electric field. *Phys. Rev.* E **82**, 050803(R).

KIRKWOOD, J.G. & RISEMAN, J. 1948 The intrinsic viscosities and diffusion constants of flexible macromolecules in solution. *J. Chem. Phys.* **16**, 565–573.

LADD, A.J.C. 2018 Electrophoresis of sheared polyelectrolytes. *Mol. Phys.* **116**, 3121–3133.

LIAO, W.-C., WATARI, N., WANG, S., HU, X., LARSON, R.G. & LEE, L.J. 2010 Conformation dependence of dna electrophoretic mobility in a converging channel. *Electrophoresis* **31**, 2813–2821.

LONG, D. & AJDARI, A. 2001 A note on the screening of hydrodynamic interactions, in electrophoresis, and in porous media. *Eur. Phys. J.* E **4**, 29–32.

MANNING, G.S. 1969 Limiting laws and counterion condensation in polyelectrolyte solutions I. Colligative properties. *J. Chem. Phys.* **51**, 924–933.

MONTES, R.J. 2018 Microfluidic concentration and purification of DNA due to electro-hydrodynamic migration. PhD thesis, University of Florida.

MONTES, R.J., BUTLER, J.E. & LADD, A.J.C. 2019a Trapping DNA with a high throughput microfluidic device. *Electrophoresis* **40**, 437–446.

MONTES, R.J., LADD, A.J.C. & BUTLER, J.E. 2019b Transverse migration and microfluidic concentration of DNA using Newtonian buffers. *Biomicrofluidics* **13** (4), 044104.

OHSHIMA, H. 1996 Henry's function for electrophoresis of a cylindrical colloidal particle. *J. Colloid Interface Sci.* **180** (1), 299–301.

PANDEY, H. & UNDERHILL, P.T. 2015 Coarse-grained model of conformation-dependent electrophoretic mobility and its influence on DNA dynamics. *Phys. Rev.* E **92**, 052301.

ROTNE, J. & PRAGER, S. 1969 Variational treatment of hydrodynamic interaction in polymers. *J. Chem. Phys.* **50**, 4831–4837.

SETARO, A.C. & UNDERHILL, P.T. 2019 Dumbbell kinetic theory for polymers in a combination of flow and external electric field. *Phys. Rev.* E **100**, 052501.

USTA, O.B., BUTLER, J.E. & LADD, A.J.C. 2007 Transverse migration of a confined polymer driven by an external force. *Phys. Rev. Lett.* **98**, 098301.

VALLEY, B.E., CROWELL, A.D., BUTLER, J.E. & LADD, A.J.C. 2020 Electro-hydrodynamic extraction of DNA from mixtures of DNA and bovine serum albumin. *Analyst* **145** (16), 5532–5538.

WARNER, H.R. 1972 Kinetic theory and rheology of dilute suspensions of finitely extendible dumbbells. *Ind. Engng Chem. Fundam.* **11**, 379–387.

ZHENG, J. & YEUNG, E.S. 2002 Anomalous radial migration of single DNA molecules in capillary electrophoresis. *Anal. Chem.* **74** (15), 4536–4547.

ZHENG, J. & YEUNG, E.S. 2003 Mechanism for the separation of large molecules based on radial migration in capillary electrophoresis. *Anal. Chem.* **75**, 3675–3680.

ZIMM, B.H. 1980 Chain molecule hydrodynamics by the Monte-Carlo method and the validity of the Kirkwood–Riseman approximation. *Macromolecules* **13**, 592–602.